Cryo-EM structure of the αvβ8 integrin reveals a mechanism for stabilizing integrin extension

Anthony Cormier[#1], **Melody G. Campbell**[#2], **Saburo Ito**[#1], **Shenping Wu**[2,3,‡], **Jianlong Lou**[4], **James Marks**[4], **Jody Baron**[5], **Stephen L. Nishimura**[1,*], and **Yifan Cheng**[2,3,*]

[1]Department of Pathology, University of California San Francisco, San Francisco, CA, USA

[2]Department of Biochemistry and Biophysics, University of California San Francisco, San Francisco, CA, USA

[3]Howard Hughes Medical Institute, University of California San Francisco, San Francisco, CA, USA

[4]Department of Anesthesia and Perioperative Care, University of California at San Francisco, San Francisco, CA, USA

[5]Department of Medicine, University of California at San Francisco, San Francisco, CA, USA

[#] These authors contributed equally to this work.

Abstract

Integrins are conformationally flexible cell surface receptors that survey the extracellular environment for their cognate ligands. Interactions with ligands are thought to be linked to global structural rearrangements involving transitions between bent, extended-closed and -open forms. Thus far, structural details are lacking for integrins in the extended conformation due to extensive flexibility between the headpiece and legs within this conformation. Here we present single-particle electron cryo-microscopy structures of human αvβ8 integrin in the extended-closed conformation, which has been considered to be a low-affinity intermediate. Our structures show the headpiece rotating about a flexible αv-knee, suggesting a ligand surveillance mechanism for integrins in their extended-closed form. Our model predicts that the extended conformation is mainly stabilized by an interface formed between flexible loops in the upper and lower domains of

*Co-corresponding authors: stephen.nishimura@ucsf.edu and yifan.cheng@ucsf.edu.
‡Current address: Department of Pharmacology, Yale University, West Haven, CT

the αv-leg. Confirming these findings with the αvβ3 integrin suggests that our model of stabilizing the extended-closed conformation is generalizable to other integrins.

Introduction

Integrins are a family of heterodimeric Type I transmembrane receptors that are sentinel sensors of the extracellular environment through mediating cell adhesive events involved in homeostasis, immunity, tissue repair and neoplasia[1]. Integrin ectodomains are composed of a α and β subunit stably joined at the α- and β-head domain, each connected to a flexible leg, which continues to a single transmembrane helix followed by a short cytoplasmic domain (Supplementary Figure 1a). Integrins utilize the flexibility of their ectodomains to bidirectionally transduce conformational signals to and from the cell interior[2]. In current models of integrin function, regulation of ligand affinity and signaling is thought to be mediated by a series of coupled motions of the ligand-binding headpiece with leg domains changing the overall shape from a bent to an extended conformation: the so called "switchblade" model (Supplementary Figure 1b)[3]. Despite extensive studies, the mechanistic structural details of integrin extension remain elusive. The opposing model proposes that integrins can regulate ligand affinity and transduce signaling entirely in a bent conformation (Supplementary Figure 1c)[4]. Furthermore, it is not known how integrins probe the extracellular milieu to find target-binding motifs in extracellular matrix proteins, cytokines and growth factors, a function not elucidated by either model.

Three major conformational states are currently proposed: bent integrins with a closed-headpiece and extended integrins with either a closed- or open-headpiece (Supplementary Figure 1). Crystal structures of integrin ectodomains reveal exclusively bent conformations (Supplementary Table 1). Negative stain electron microscopy (ns-EM) images of numerous integrin heterodimers exhibit all three conformational states with ligand occupancy favoring the extended-open conformation (Supplementary Table 1). These studies mainly support the prevailing hypothesis that the high-affinity state has an extended-open conformation[5].

For the αvβ8 integrin by ns-EM only the extended-closed form has been observed either alone or in association with ligand[6,7]. These findings are inconsistent with both the bent and the switchblade models and suggest that the αvβ8 integrin functions entirely in the extended-closed form (Supplementary Figure 1d). The relative conformational homogeneity of αvβ8 makes it an ideal target for structural studies of an integrin in the extended conformation. Here we present single-particle electron cryo-microscopy (cryo-EM) structures of the αvβ8 integrin in complex with two fragments of antigen binding (Fabs) to reveal an integrin in a range of extended conformations with unprecedented clarity. We achieve an overall resolution of 6.4 Å, with a resolution of 4.8Å in the headpiece. The motion between the headpiece and the leg suggests a mechanism by which integrin headpieces survey extracellular surfaces for ligands. Our structures predict the interactions between αv-thigh and calf-1 domains in this extended conformation, which is confirmed with rationally designed αvβ3 mutants.

Results

Cryo-EM structures of the αvβ8 integrin

Integrins in an extended conformation have not been crystallized. Current single particle EM structures do not have sufficient detail to provide insights into integrin extension or surveillance mechanisms (Supplementary Table 1). Even with the recent advances in single particle cryo-EM[8], determining high resolution integrin structures remains challenging. The main technical barriers are the low mass density, asymmetry and extreme conformational flexibility, all of which conspire to hinder accurate image alignment and conformational classification[9]. To mitigate these challenges, we use two different monoclonal Fabs (8B8 and 68) directed at the headpiece of the αvβ8 integrin to increase the molecular mass and facilitate more accurate image alignment[10]. Neither Fab alters αvβ8 function, with 8B8 directed at the αv-head and 68 to the β8 βI-domain[6]. With this combination of Fabs, we determine the structure of the αvβ8–8B8–68 complex to an overall resolution of 6.4 Å, in which the integrin is in the extended-closed conformation (Figure 1a, Supplementary Figure 2 **and** Supplementary Table 2). An atomic model of the αvβ8 integrin in the extended conformation was obtained by fitting homology models of individual domains (based on available crystal structures of integrin αvβ3) into the cryo-EM density map. Subsequently, the model was iteratively rebuilt and refined into the density using Phenix[11] and Rosetta[12] (Figure 1b). At this resolution, the boundaries for all the individual domains in the αv leg and β8 headpiece are clearly defined, with well resolved secondary structural features including all α-helices and many β-sheets (Figure 1a, b).

The inherent conformational flexibilities of integrin leg domains relative to the headpiece and the flexibility of the Fab constant relative to the variable domains (which together account for ~42% of the total mass of the complex) compromise the accuracy of image alignment and limit the overall resolution. By masking out the leg and the constant domains of the Fabs we improve the resolution of the headpiece to 4.8 Å (Figure 1c; Supplementary Table 2; Supplementary Figure 2c, f). At this improved resolution, densities of some bulky side chains and glycans of all predicted N-linked glycosylation sites in the headpiece are clearly resolved serving as excellent landmarks for model building and validation (Figure 1d, e; Supplementary Table 3).

Head domain motions: the sunflower model

When image alignment is focused on the headpiece, the leg densities become very weak, indicating the relative flexibility between the head and legs. 3D classification reveals six conformational snapshots, each at sub-nanometer resolution with improved leg density (Supplementary Figure 3). To approximate the motion of a membrane anchored integrin, we align the αv-lower legs of each subclass with each other, revealing different angular positions of the αvβ8 headpiece as it tilts relative to the leg domains (Figure 2a – c). Individual subclasses reveal complex twisting and angular motions of the headpiece which are associated with varying degrees of contact between the β8 upper and lower legs with the αv-leg. The range of motion of the headpiece is approximately 30° estimated from the differences between subclasses (i) and (v), the least and most extended subclasses, respectively (Figure 2a – c).

The intrinsic motion of the headpiece of an integrin joined to flexible legs anchored on the plasma membrane would facilitate surveillance of the extracellular space for ligand detection. The overall effect is that the αvβ8 head samples an elliptical conic-space similar to a sunflower as it moves during the day (Supplementary Video 1). Our data provide structural insight into how a single integrin samples a large space and this motion is presumably beneficial for ligand detection.

Loss of β8 leg contacts with the αv-leg favors full receptor extension

The changes in β8 leg density in the six subclasses suggest a role for the β8 leg in the sunflower motion. In subclass (i), the β8 leg density is apparent as a continuous density between the β8 upper leg which contacts the αv-thigh domain and then continues along the αv-lower leg (Figure 2b). The αvβ8 headpiece movement through subclasses (ii-vi) involves loosening of the contacts that the β8 upper leg makes with the αv-thigh and αv-calf-1 domains in subclass (i) (Figure 2a – c). Likewise, the β8 lower leg density is strongest in subclass (i) and is weaker in subclasses (ii-vi), suggesting that the β8 leg loses contact with the αv-leg as αvβ8 maximally extends (Supplementary Figure 4).

The resolution of the density map does not permit modeling of the individual domains of the β8 leg. However, the density map of subclass (i) allows placement of the β8 Psi-EGF1 domain, which forms the lower portion of the upper β-subunit leg in the integrin headpiece and ectodomain crystal structures, in contact with the C-terminal αv-thigh domain (Figure 2d). Contact of the Psi-EGF1 domain with the αv-subunit is not observed in subclasses (iii-vi) (Figure 2e). Overall, these data suggest that domain contacts between the αv- and β8-legs are not required to maintain the extended conformation.

Following this result, we further hypothesize that in all αv integrins the αv-leg alone is sufficient to maintain an extended conformation. To test the role of β-leg in integrin extension, we generate a mutant αvβ3 integrin ectodomain truncated at the β3 EGF2 domain (Figure 3). If the β3 lower leg is required for extension, the truncation mutant would be predicted to destabilize extension and favor bending. However, ns-EM demonstrates that the lower-leg β3 deletion mutant has a slight decrease in bent forms compared with the wild type αvβ3 integrin ectodomain, suggesting that the β-lower leg does not directly contribute to extension of the αv-leg (Figure 3a–f).

The αv-hinge

Comparison of the overall and sub-classified cryo-EM density maps confirm that the entire lower αv-leg is more or less a rigid body, with the major point of motion occurring between the lower αv-thigh domain of the upper αv-leg and the calf-1 domain of the αv-lower leg (Figure 2a–c). In our model the αv-thigh domain interfaces extensively with the αv-calf-1 domain through interactions between a loop in the αv-thigh domain and three loops in the calf-1 domain (Figure 4a). These loops are not in contact in the crystal structure of αvβ3 in the bent conformation[13]. Also, a loop between the C-terminal thigh and N-terminal calf-1 domain designated as the knee region in αvβ3 crystal structures does not participate in the αv-thigh-calf-1 interface in the extended conformation (Figure 2d, e). These two observations suggest a rearrangement of domains from bent to extended conformations so

that new interactions are formed to stabilize the extended conformation. Sequence alignment of the PS2 subfamily of integrin α subunits shows that these predicted interacting loops are highly conserved (Figure 4b). To validate our prediction and to generalize our model to other αv-integrins, we introduce two cysteine residues (S546C and N685C) into two opposing loops of the αv integrin subunit, one in the thigh loop and the other in loop 2 of the calf-1 domain (Figure 3g, 4a), which henceforth is referred to as the αvc-c mutant. When paired with either the β8 or β3 subunits it forms two different functional integrin heterodimers. If our model of the extended αv leg is correct, a disulfide bond will form between these two cysteine residues and lock the αv leg into an extended conformation. Consequentially, when expressed on the cell surface, αvc-c would be predicted to enhance the function of integrin αvβ3, by relieving steric hindrance, but not the function of αvβ8, which is already extended.

Ns-EM of the mutant αvc-cβ3 ectodomain reveals only extended but no bent integrins (Figure 3g – i). In comparison, ns-EM of the wild type αvβ3 integrin ectodomain shows all forms (Figure 3a – c). To confirm our findings *in vivo*, we expressed the full-length mutant and wild type human αvβ3 integrins on the cell surface of Chinese Hamster Ovary (CHO) cells. These cells are sorted to have uniform and equal expression of the mutant and wild-type αv in addition to β3 subunits (Figure 5a). The αvc-cβ3 integrin has increased basal exposure of ligand-induced-binding-site (LIBS) epitopes consistent with a constitutively extended conformation (Figure 5a). Furthermore, the αvc-cβ3 integrin displays increased ability to mediate cell adhesion to its ligand, vitronectin, than the wild type αvβ3, both in basal and activating cation conditions (Figure 5b). As expected, the αvc-cβ8 mutant and wild type human αvβ8 integrins expressed on CHO cells bind equally to its ligand, latent TGF-β (Figure 5c), and show no preferential binding under the activating cation conditions, consistent with previous studies[6]. The increased ability of the αvc-cβ3 integrin to mediate cell adhesion is not due to increased binding affinity, since the mutant and wild type integrin ectodomains bind equally to their ligands in both basal and activating cation conditions (Supplementary Figure 5a).

Discussion

The integrin αvβ8 is functionally specialized to bind latent forms of the multifunctional cytokines TGF-β1 and TGF-β3 (L-TGF-β)[14,15]. The majority of L-TGF-β is not freely diffusible but covalently attached to extracellular matrix or to the cell surface via L-TGF-β binding proteins (i.e. LTBP1) or cell surface scaffolding proteins (i.e. GARP)[16,17]. Binding of αvβ8 to cell or matrix-expressed L-TGF-β results in the release of active TGF-β, a process essential for the homeostatic and pathologic functions of TGF-β *in vivo*[18]. The αvβ8 integrin may have evolved, among the five integrins that share the αv-subunit, to bias its conformational range towards the extended-closed form to increase the chance to encounter L-TGF-β expressed on an opposing cell or matrix.

Despite pairing with the same αv-subunit, αvβ3 can bend while αvβ8 does not, indicating that the β-subunit plays a role in integrin conformational dynamics. Our cryo-EM data suggest that contacts between the αv and β8 lower legs are critical in the tilting of the headpiece during the sunflower motion and that separation of the αv and β8 lower legs favors further extension. As such, the tilting of the αvβ8 headpiece may represent an

analogue of the bent form of αvβ3, the differences in the magnitude of bending driven by differences within the β8 lower leg. Experimental mutagenesis or naturally occurring disease causing mutations in the β3 lower leg cause constitutive activation and exposure of LIBS epitopes indicating that such mutations cause extension of the $α_{iib}$β3 integrin[19,20]. These β3 mutations often occur in conserved cysteines, which form disulfide loops and are critical determinates of the EGF domain structure of the β3 lower leg[20]. The β8 lower leg lacks two of these conserved disulfide pairs in the EGF3 and β-tail domains (Supplementary Figure 5c). One possibility is that the β8 lower leg has lost its ability to stabilize the bent conformation, which raises the hypothesis that other integrin β-subunit lower legs stabilize the bent conformation. An alternate hypothesis has been proposed that the β-lower leg contributes to extension via a disulfide loop of EGF2 at the junction between the upper and lower legs of integrin β-subunits that acts as an entropic spring shifting the conformational equilibrium towards extension[21]. To test these hypotheses, we remove the lower leg of the β3 subunit containing the entropic spring and find that the conformational ensemble of the αvβ3 truncation mutant is somewhat biased towards the extended-open conformation. This result favors the hypothesis that the β-lower leg stabilizes the bent conformation.

Our model of the extended αv-leg predicts that two loops between the αv-thigh and αv-calf-1 domain contribute to stabilizing the extended conformation. We validated this model, and suggest that the extended conformation for a α-integrin subunit is stable without contribution from the β lower leg. Furthermore, our data suggest that the β-leg does not cause the extended conformation. Based on our data, we hypothesized that the transition from the bent to extended closed conformation requires disrupting or weakening α-β lower leg interactions, which releases the integrin to the extended conformation. Sequence comparison suggests that this model of integrin extension could apply at the very least to the closely related integrin α-subunits, $α_{iib}$, α5 and α8, which are strikingly homologous in the interacting loops of the α-thigh and α-calf-1 domains.

αvβ8 only assumes the extended-closed conformation yet efficiently binds to and activates L-TGF-β, indicating that the extended-closed conformation of αvβ8 is functional. Here we generalize this finding to the αvβ3 integrin by providing evidence that the extended-closed form of αvβ3 is also functional. This conclusion is made based on the fact that when expressed on the cell surface the αvc-cβ3 mutant exhibits increased basal adhesion compared to WT αvβ3, while the soluble αvc-cβ3 and WT αvβ3 ectodomains exhibit identical basal ligand binding. If the regulation of ligand affinity of the membrane bound and ectodomain-only forms of αvβ3 are similar, our results suggest that the constitutively extended αvc-cβ3 is mainly in an extended-closed, low-affinity state and that the functional advantage gained by extension when expressed on the cell surface is accessibility to ligand, not increased affinity. These findings raise the possibility that the extended-closed conformation of other integrins is biologically important.

In summary, cryo-EM is an advantageous method for determining multiple snapshots at sub-nanometer resolution of integrins across their dynamic conformational range. Characterizing the motion of αvβ8 has provided valuable insights into the integrin extension mechanism and has provided a model for ligand surveillance, which we found to also be applicable to

αvβ3. These data suggest that this mechanism for stabilizing integrin extension could be generalizable to other integrins.

Accession Codes:

Cryo-EM density maps are deposited in EMDB with accession code EMD-7939. The related coordinate is deposited to Protein Data Bank with accession codes 6DJP.

Online Methods

Cell lines and Reagents

The antibodies 8B8, 68, AP3, AP5, LIBS1, LIBS6 have been previously described[6,22,23]. Human embryonic kidney 293 (HEK293) cells were obtained from the American Tissue Type Collection (ATCC, Manassus, VA). CHOLec 3.2.8.1 cells were provided by Pamela Stanley[24]. Truncated recombinant human vitronectin N-terminal fragment (VTN-N) was purchased from Thermo Fisher scientific (Waltham, MA). Cell culture media and antibiotics were prepared by the University of California, San Francisco Cell Culture Facility using deionized water and analytical grade reagents. Fetal calf serum was obtained from Invitrogen (Carlsbad, CA). The CHOlec 3.2.8.1 cell line was functionally verified by production of hypoglycosylated recombinant protein by SDS-PAGE. The cell line was not tested for mycoplasma contamination.

Protein expression and purification

Wild-type and mutant recombinant human integrin αvβ8 and αvβ3 truncated at the junction of the ectodomains and transmembrane domains in pcDNA1neo[25] were expressed using stably expressing CHOLec 3.2.8.1 cells grown in bioreactors (for structural studies), or transiently transfected HEK293 cells (for biochemical characterization). Purification was carried out by affinity chromatography using a Protein G – 8B8 column followed by size exclusion chromatography (Superdex 200 Increase 10/300 GL, GE Healthcare) in 20mM Tris-HCL pH 7.5, 150 mM NaCl, 1mM $CaCl_2$ and 1mM $MgCl_2$.

Antibodies were purified as described previously[6]. 8B8 and 68 fragments were generated by papain digestion (Pierce) of the IgG followed by Protein-A Agarose (Millipore) incubation to remove Fc fragments and intact antibodies.

The homogeneity and purity of all protein preparations were verified by SDS-PAGE stained with Coomassie blue and protein concentrations were measured by microbicinchoninic acid assay (Pierce). To prepare integrin-Fab complexes, 100 μg of recombinant αvβ8 was incubated in a 2-fold molar excess of each Fab, incubated at room temperature for 30 min, subjected to size exclusion chromatography and concentrated to 6 to 9 mg/ml. Porcine L-TGF-β was expressed and purified as described[26].

Ns-EM sample preparation, data acquisition and analysis

Grids of negatively stained integrin samples were prepared following established protocols[27]. Specifically, 2.5 μl of purified truncated αvβ3, αvβ3HP, αvc-cβ3 sample with a concentration of ~0.02 mg/ml were applied to glow-discharged carbon-coated copper grids,

washed, stained with 0.75% (w/v) uranylformate, and aspirated to dryness[6]. Negatively stained grids were imaged on a Tecnai T12 electron microscope (FEI Company) equipped with a LaB6 filament and operating at a 120 kV acceleration voltage. Images were recorded at a nominal magnification of 52,000x and a defocus of −1.5 μm using a 4K CCD camera (UltraScan 4000, Gatan, Inc., Pleasanton, CA), with a corresponding pixel size 2.21 Å on the specimen. Images were 2 × 2 binned for particle picking and further processing. Particles were picked using reference-free methods as implemented in Gautomatch (http://www.mrc-lmb.cam.ac.uk/kzhang/Gautomatch) and further processed using the Relion pipeline[28].

Cryo-EM sample preparation, data acquisition and analysis

For cryo-EM grid preparation, 3 μl of purified αvβ8–8B8–68 complex (6.8 mg/ml concentration) was applied to Quantifoil grids (holey carbon film with 1.2 μm hole size and 1.3 μm hole spacing on 400-mesh Cu grid) glow-discharged for 60 seconds at 15 mA, blotted with a Vitrobot Mark III (FEI Company) using 3.5–4.5 second blotting time with 100% humidity at 20°C, and plunge-frozen in liquid ethane cooled by liquid nitrogen.

Cryo-EM images of frozen hydrated αvβ8–8B8–68 complexes were collected on a TF30 Polara electron microscope (FEI Company) equipped with a field emission electron source and operated at 300kV. Images were recorded at a nominal magnification of 31,000x using a K2 Summit direct electron detector camera (Gatan) operated in super-resolution mode following an established protocol[29]. The microscope settings are extraction voltage 4200eV, gun lens 1, spotsize 3, a 30 μm C2 aperture and a 100 μm objective aperture. Data were manually collected using UCSFImage4[30] or SerialEM[31], using a nominal defocus range of −1.8 to −2.8 μm. The calibrated physical pixel size is 1.2156 Å at specimen and a dose rate of 10.12 e⁻/pixel. A total dose of 41 e⁻/Å^2 was fractionated over 30 frames during the 6s exposures. From the cryo-EM images, particles do not have preferred orientation in vitreous ice, but they are only found in thick ice and sparsely distributed. A total of 2174 movies were collected over three sessions, however only 713 movies (collected during a single session) were used for the final map.

Dose fractionated super-resolution image stacks were motion corrected and binned 2 × 2 by Fourier cropping using MotionCor2[32]. Motion corrected sums without dose-weighting were used for contrast transfer function (CTF) determination using GCTF[33]. The relatively low signal to noise ratio in Fourier power spectra, due to sparsely distributed particles in thick ice, limits the accuracy of CTF estimation. 144,005 particles were picked using the reference-free method in Gautomatch and boxed out in Relion 2.0 with a box size of 320 pixels and binned to 64 pixels. Upon micrograph inspection, we note that many of these picks were 'false positives' and do not represent particles but rather ice or debris. This is likely due to the reference-free picking approach. After two rounds of 2D alignment and classification in Relion 2.0[28], particles were re-extracted and binned to 128 pixel to generate *ab initio* initial models using CryoSPARC[34]. After 3D alignment and classification in Relion 2.0 to further sort out ideal particles from junk, this new smaller subset of particles (17,442) were re-extracted using dose-weighted micrographs and binned to a final box size of 256 pixels (1.67 Å/pixel). Using one of the models generated during 3D classification low-pass filtered to 20 Å as an initial model, initial angles and shifts were determined in Relion 2.0.

Frealign 9[35] in mode 1 was used for subsequent refinement and reconstruction. During the refinement, only data up to a resolution of 8 Å were used to avoid possible over-fitting and bias in the FSC curves at higher resolution. For the αvβ8–8B8–68 complex, the resolution of the overall map was estimated to be 6.4Å. Subsequently, a soft mask was generated to exclude the constant domains of both Fabs as well as Calf1 and Calf2 of the α subunit and the Psi-EGF1 domains of the β subunit. This improved the resolution of the αvβ8–8B8–68 complex to 4.8Å (resolution limited to 6Å in Frealign). We speculate that the accuracy of CTF estimation as well as thick ice are contributing factors that limit the resolution. For the six complexes showing leg motion, the processing schematic is described in Supplementary Figure 3 and the resolution during refinement was limited to 10Å in all cases.

Resolutions were determined using FSC = 0.143 criterion[36]. All post processing including mask generation, filtering, sharpening, and masked FSC estimation were done using Relion 2.0. Local resolution was estimated in Bsoft blocres[37]. Map to model FSC was calculated in Rosetta. Images were rendered in UCSF Chimera[38] and Pymol [39], movie was rendered in UCSF Chimera.

Model Building and refinement

The atomic model of the αv headpiece from the crystal structure of αvβ3 (PDB: 3IJE) with glycans removed was fitted to the cryo-EM density of αvβ8–8B8–68 complex as a rigid body. An atomic model of the β8 headpiece was generated by rigid body fitting of a homology model based on the same crystal structure (3IJE) using Modeller[40] into the cryo-EM map. Atomic models of Fabs were generated with Rosetta Antibody using multiple-template grafting and H3 loop modelization[12] based on the primary sequence of their V_h and V_k. The models for Fab 68 and Fab 8B8 were then fitted as a rigid body to the map. Prototypical CHOLec glycans were added back to the model at the solvent exposed N-glycosylation consensus sites using GLYCAM[41]. The sugar base of glycans were trimmed to fit into the corresponding densities. After rigid body fitting, models were manually adjusted in COOT[42], followed by real space refinement using Phenix[11] and Rosetta.

Integrin mutants constructs

To construct the truncated human αvc-c mutant, splice overlap extension PCR was used. Mutagenic primers are included in Supplementary Table 4; The resulting amplicon was cut with PstI and SphI and ligated into αv truncated pcDM8 cut with the same enzymes[43]. To make the full-length αvc-c mutant, truncated αvc-c pcDM8 was cut with BstEII and SphI and ligated into αv full length pcDM8 cut with the same enzymes.

The human β3 HP mutant was amplified using primers listed in Supplementary Table 4 followed by cutting with BamH1 and XhoI and ligating into human truncated β3 pcDNA1neo cut with the same enzymes[44]. All constructs were verified by sequencing.

Ligand binding, Cell adhesion assays and Cell staining

For ligand binding assays, ELISA plates were coated with 0.5µg/ml of L-TGF-β (for αvβ8 WT and αvc-cβ8) or vitronectin-N (for αvβ3 WT and αvc-cβ3), blocked with 5% BSA in PBS for 1 hour, truncated integrin was allowed to bind for 2 hours at RT and bound integrin

was detected with 8B8-biotin and streptavidin-HRP. For cell adhesion assays, ELISA plates were coated with various concentrations of vitronectin-N, or L-TGF-β, blocked with PBS with 5% BSA for 1 hour and then 50000 αvβ3, αvβ8, or αvc-cβ3 or αvc-cβ8 CHOLec 3.2.8.1 cells were allowed to adhere to wells for 30 min at RT in the presence of 1mM Ca^{2+} and 1mM Mg^{2+} or 0.2mM Mn^{2+}. Cell staining and flow cytometry was performed as previously described[6]

Sequence alignments

Multiple protein sequence alignments for integrins were generated using Tcoffee[45].

Statistics

ELISA data are reported as means ± s.e.m. All statistical analyses were performed using the software package Prism 4.0b (GraphPad Software, San Diego, CA).

Supplementary Material

Refer to Web version on PubMed Central for supplementary material.

Acknowledgements:

References:

1. Hynes RO The emergence of integrins: a personal and historical perspective. Matrix Biol 23, 333–340, doi:10.1016/j.matbio.2004.08.001 (2004). [PubMed: 15533754]

2. Campbell ID & Humphries MJ Integrin structure, activation, and interactions. Cold Spring Harb Perspect Biol 3, doi:10.1101/cshperspect.a004994 (2011).

3. Takagi J, Petre BM, Walz T & Springer TA Global conformational rearrangements in integrin extracellular domains in outside-in and inside-out signaling. Cell 110, 599–511 (2002). [PubMed: 12230977]

4. Xiong JP et al. Crystal structure of the complete integrin alphaVbeta3 ectodomain plus an alpha/beta transmembrane fragment. J Cell Biol 186, 589–600, doi:10.1083/jcb.200905085 (2009). [PubMed: 19704023]

5. Luo BH, Carman CV & Springer TA Structural basis of integrin regulation and signaling. Annu Rev Immunol 25, 619–647, doi:10.1146/annurev.immunol.25.022106.141618 (2007). [PubMed: 17201681]

6. Minagawa S et al. Selective targeting of TGF-beta activation to treat fibroinflammatory airway disease. Sci Transl Med 6, 241ra279, doi:10.1126/scitranslmed.3008074 (2014).

7. Wang J et al. Atypical interactions of integrin alphaVbeta8 with pro-TGF-beta1. Proc Natl Acad Sci U S A 114, E4168–E4174, doi:10.1073/pnas.1705129114 (2017). [PubMed: 28484027]

8. Cheng Y Single-Particle Cryo-EM at Crystallographic Resolution. Cell 161, 450–457, doi:10.1016/j.cell.2015.03.049 (2015). [PubMed: 25910205]

9. Cheng Y, Grigorieff N, Penczek PA & Walz T A primer to single-particle cryo-electron microscopy. Cell 161, 438–449, doi:10.1016/j.cell.2015.03.050 (2015). [PubMed: 25910204]

10. Wu S et al. Fabs enable single particle cryoEM studies of small proteins. Structure 20, 582–592, doi:10.1016/j.str.2012.02.017 (2012). [PubMed: 22483106]

11. Adams PD et al. PHENIX: a comprehensive Python-based system for macromolecular structure solution. Acta Crystallogr D Biol Crystallogr 66, 213–221, doi:10.1107/S0907444909052925 (2010). [PubMed: 20124702]

12. Lyskov S et al. Serverification of molecular modeling applications: the Rosetta Online Server that Includes Everyone (ROSIE). PLoS One 8, e63906, doi:10.1371/journal.pone.0063906 (2013). [PubMed: 23717507]

13. Xiong JP et al. Crystal structure of the extracellular segment of integrin alpha Vbeta3 in complex with an Arg-Gly-Asp ligand. Science 296, 151–155, doi:10.1126/science.1069040 (2002). [PubMed: 11884718]

14. Mu D et al. The integrin alpha(v)beta8 mediates epithelial homeostasis through MT1-MMP-dependent activation of TGF-beta1. J Cell Biol 157, 493–507, doi:10.1083/jcb.200109100 (2002). [PubMed: 11970960]

15. Ozawa A et al. Molecular Basis of the Ligand Binding Specificity of alphavbeta8 Integrin. J Biol Chem 291, 11551–11565, doi:10.1074/jbc.M116.719138 (2016). [PubMed: 27033701]

16. Robertson IB et al. Latent TGF-beta-binding proteins. Matrix Biol 47, 44–53, doi:10.1016/j.matbio.2015.05.005 (2015). [PubMed: 25960419]

17. Tran DQ et al. GARP (LRRC32) is essential for the surface expression of latent TGF-beta on platelets and activated FOXP3+ regulatory T cells. Proc Natl Acad Sci U S A 106, 13445–13450, doi:10.1073/pnas.0901944106 (2009). [PubMed: 19651619]

18. Nishimura SL Integrin-mediated transforming growth factor-beta activation, a potential therapeutic target in fibrogenic disorders. Am J Pathol 175, 1362–1370, doi:10.2353/ajpath.2009.090393 (2009). [PubMed: 19729474]

19. Kamata T et al. Critical cysteine residues for regulation of integrin alphaIIbbeta3 are clustered in the epidermal growth factor domains of the beta3 subunit. Biochem J 378, 1079–1082, doi:10.1042/BJ20031701 (2004). [PubMed: 14690453]

20. Mor-Cohen R et al. Disulfide bond disruption by a beta 3-Cys549Arg mutation in six Jordanian families with Glanzmann thrombasthenia causes diminished production of constitutively active alpha IIb beta 3. Thromb Haemost 98, 1257–1265 (2007). [PubMed: 18064323]

21. Smagghe BJ, Huang PS, Ban YE, Baker D & Springer TA Modulation of integrin activation by an entropic spring in the {beta}-knee. J Biol Chem 285, 32954–32966, doi:10.1074/jbc.M110.145177 (2010). [PubMed: 20670939]

22. Frelinger AL, 3rd, Du XP, Plow EF & Ginsberg MH Monoclonal antibodies to ligand-occupied conformers of integrin alpha IIb beta 3 (glycoprotein IIb-IIIa) alter receptor affinity, specificity, and function. J Biol Chem 266, 17106–17111 (1991). [PubMed: 1894607]

23. Honda S et al. Topography of ligand-induced binding sites, including a novel cation-sensitive epitope (AP5) at the amino terminus, of the human integrin beta 3 subunit. J Biol Chem 270, 11947–11954 (1995). [PubMed: 7538128]

24. Stanley P Chinese hamster ovary cell mutants with multiple glycosylation defects for production of glycoproteins with minimal carbohydrate heterogeneity. Mol Cell Biol 9, 377–383 (1989). [PubMed: 2710109]

25. Nishimura SL, Sheppard D & Pytela R Integrin alpha v beta 8. Interaction with vitronectin and functional divergence of the beta 8 cytoplasmic domain. J Biol Chem 269, 28708–28715 (1994). [PubMed: 7525578]

26. Shi M et al. Latent TGF-beta structure and activation. Nature 474, 343–349, doi:10.1038/nature10152 (2011). [PubMed: 21677751]

27. Booth DS, Avila-Sakar A & Cheng Y Visualizing proteins and macromolecular complexes by negative stain EM: from grid preparation to image acquisition. J Vis Exp, doi:10.3791/3227 (2011).

28. Scheres SH RELION: implementation of a Bayesian approach to cryo-EM structure determination. J Struct Biol 180, 519–530, doi:10.1016/j.jsb.2012.09.006 (2012). [PubMed: 23000701]

29. Li X et al. Electron counting and beam-induced motion correction enable near-atomic-resolution single-particle cryo-EM. Nat Methods 10, 584–590, doi:10.1038/nmeth.2472 (2013). [PubMed: 23644547]

30. Li X, Zheng S, Agard DA & Cheng Y Asynchronous data acquisition and on-the-fly analysis of dose fractionated cryoEM images by UCSFImage. J Struct Biol 192, 174–178, doi:10.1016/j.jsb. 2015.09.003 (2015). [PubMed: 26370395]

31. Mastronarde DN Automated electron microscope tomography using robust prediction of specimen movements. J Struct Biol 152, 36–51, doi:10.1016/j.jsb.2005.07.007 (2005). [PubMed: 16182563]

32. Zheng SQ et al. MotionCor2: anisotropic correction of beam-induced motion for improved cryo-electron microscopy. Nat Methods 14, 331–332, doi:10.1038/nmeth.4193 (2017). [PubMed: 28250466]

33. Zhang K Gctf: Real-time CTF determination and correction. J Struct Biol 193, 1–12, doi:10.1016/ j.jsb.2015.11.003 (2016). [PubMed: 26592709]

34. Punjani A, Brubaker MA & Fleet DJ Building Proteins in a Day: Efficient 3D Molecular Structure Estimation with Electron Cryomicroscopy. IEEE Trans Pattern Anal Mach Intell 39, 706–718, doi: 10.1109/TPAMI.2016.2627573 (2017). [PubMed: 27849524]

35. Grigorieff N Frealign: An Exploratory Tool for Single-Particle Cryo-EM. Methods Enzymol 579, 191–226, doi:10.1016/bs.mie.2016.04.013 (2016). [PubMed: 27572728]

36. Rosenthal PB & Henderson R Optimal determination of particle orientation, absolute hand, and contrast loss in single-particle electron cryomicroscopy. J Mol Biol 333, 721–745 (2003). [PubMed: 14568533]

37. Heymann JB & Belnap DM Bsoft: image processing and molecular modeling for electron microscopy. J Struct Biol 157, 3–18, doi:10.1016/j.jsb.2006.06.006 (2007). [PubMed: 17011211]

38. Pettersen EF et al. UCSF Chimera--a visualization system for exploratory research and analysis. J Comput Chem 25, 1605–1612, doi:10.1002/jcc.20084 (2004). [PubMed: 15264254]

39. DeLano WL Pymol: An open-source molecular graphics tool. CCP4 Newsletter On Protein Crystallography 40, 82–92 (2002).

40. Webb B & Sali A Comparative Protein Structure Modeling Using MODELLER. Curr Protoc Bioinformatics 47, 5 6 1–32, doi:10.1002/0471250953.bi0506s47 (2014). [PubMed: 25199792]

41. Singh A et al. Extension and validation of the GLYCAM force field parameters for modeling glycosaminoglycans. Can J Chem 94, 927–935, doi:10.1139/cjc-2015-0606 (2016). [PubMed: 28603292]

42. Emsley P, Lohkamp B, Scott WG & Cowtan K Features and development of Coot. Acta Crystallogr D Biol Crystallogr 66, 486–501, doi:10.1107/S0907444910007493 (2010). [PubMed: 20383002]

43. Weinacker A et al. Role of the integrin alpha v beta 6 in cell attachment to fibronectin. Heterologous expression of intact and secreted forms of the receptor. J Biol Chem 269, 6940–6948 (1994). [PubMed: 8120056]

44. Gline SE, Cambier S, Govaerts C & Nishimura SLA 50-A separation of the integrin alpha v beta 3 extracellular domain C termini reveals an intermediate activation state. J Biol Chem 279, 54567–54572, doi:10.1074/jbc.M406582200 (2004). [PubMed: 15475365]

45. Notredame C, Higgins DG & Heringa J T-Coffee: A novel method for fast and accurate multiple sequence alignment. J Mol Biol 302, 205–217, doi:10.1006/jmbi.2000.4042 (2000). [PubMed: 10964570]
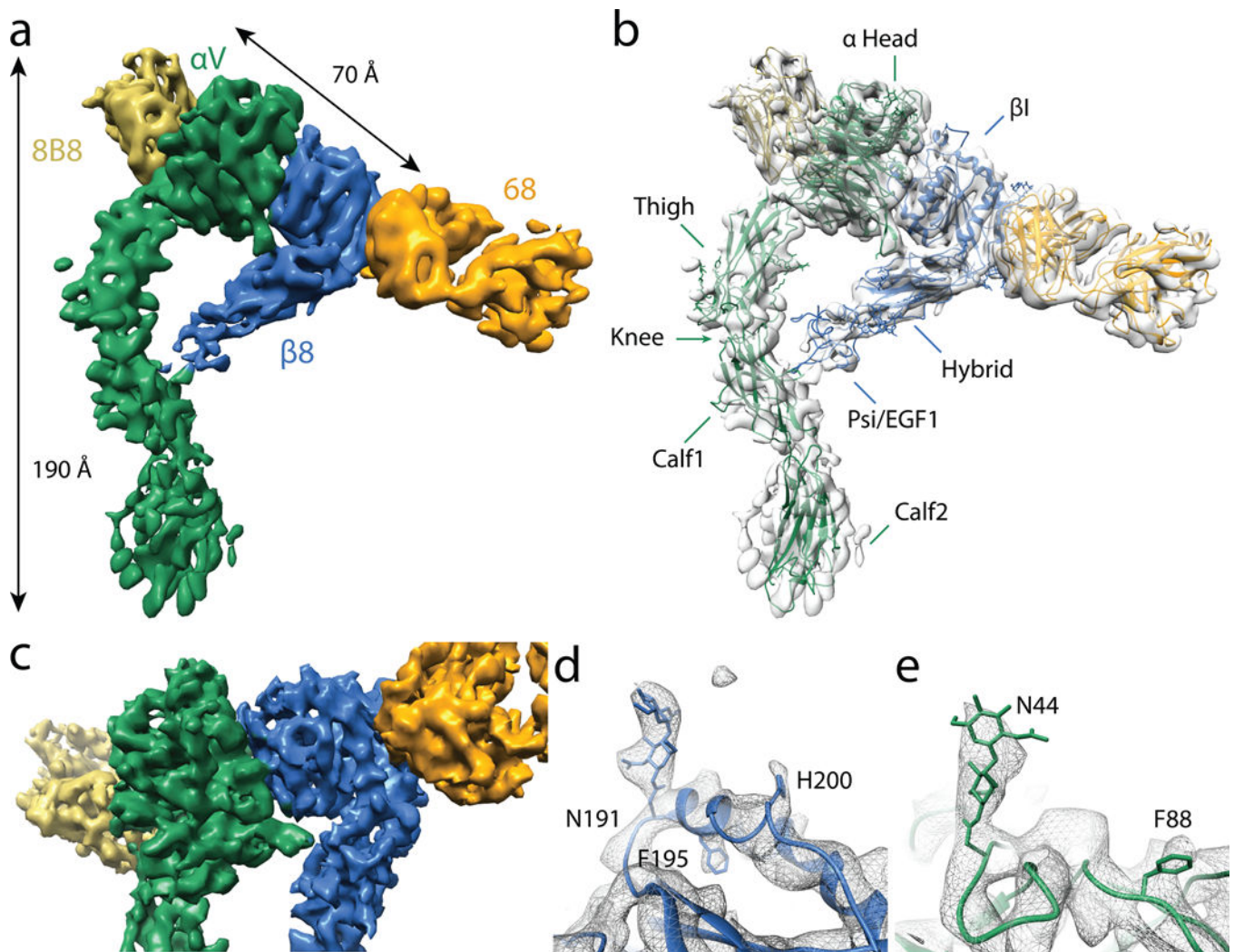
**Figure 1 |. Structure of the αvβ8 integrin in extended-closed conformation.**
**a**, Cryo-EM structure of αvβ8–8B8–68 complex at a global 6.4Å resolution. The axial and head-domain dimensions are shown. **b**, The atomic model shown in ribbon format and fit into the EM density. Names of individual domains are shown. The headpiece consists of the αv-head, thigh, β8 βI, hybrid and Psi-EGF1 domains. **c**, Close up of the headpiece, which is resolved to 4.8Å through focused alignment. **d**, Close up of the β8 headpiece showing the glycan attached to N191 as well as the two bulky sidechains H200 and F195. **e**, Close up of the αv headpiece showing the glycan attached to N44 and the bulky side chain F88. The color code is: αv-green; β8-blue; Fab 68-orange; Fab 8B8-yellow.
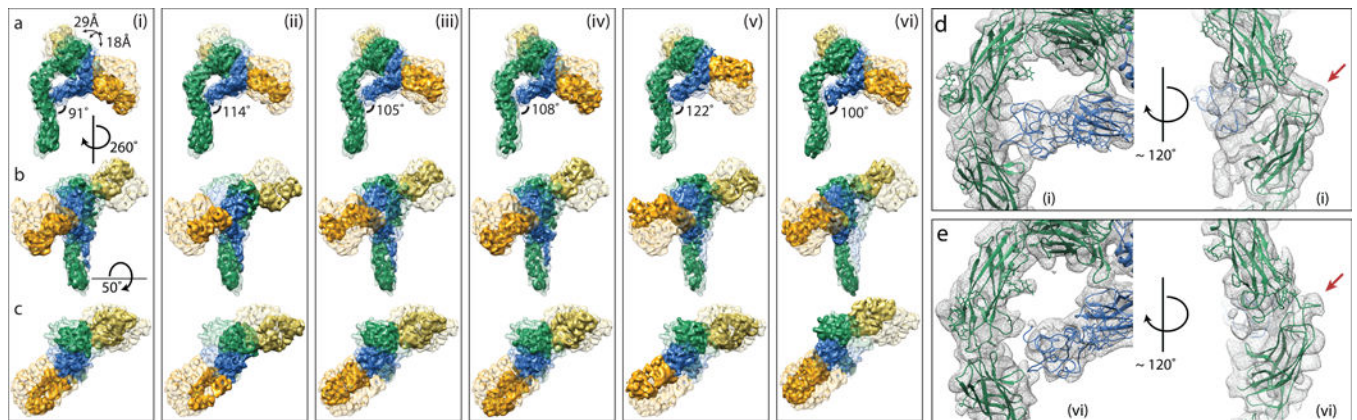
Figure 2 |. The αvβ8 headpiece rotates about a flexible αv-knee to survey the environment
a to **c,** A single dataset of integrin αvβ8–8B8–68 complex is used to generate six independently-refined integrin structural subclasses (labeled **i** to **vi**). These structures are aligned to each other based on the calf regions of the αv-lower leg. Each vertical panel shows three views of each subclass in solid color and the other five at 40% transparency. These six conformational snapshots represent the range of continuous motion of the αvβ8 headpiece. The overall motion of the headpiece is qualitatively similar to the path of a sunflower following the sun, presumably to expand the sampling area. Models (i) and (vi) represent the most extreme conformations measured as the angle of the hybrid domain with the αv-lower leg. **d** and **e,** Close-up front and side views of the αv-knee and point of contact between the Psi-EGF1 and the αv-leg shown as the atomic models in ribbon diagram fitted to the density map of subclass (i) (**d**) and (vi) (**e**). Arrows indicate the αv-knee region. The color code is: αv-green; β8-blue; Fab 68-orange; Fab 8B8-yellow.
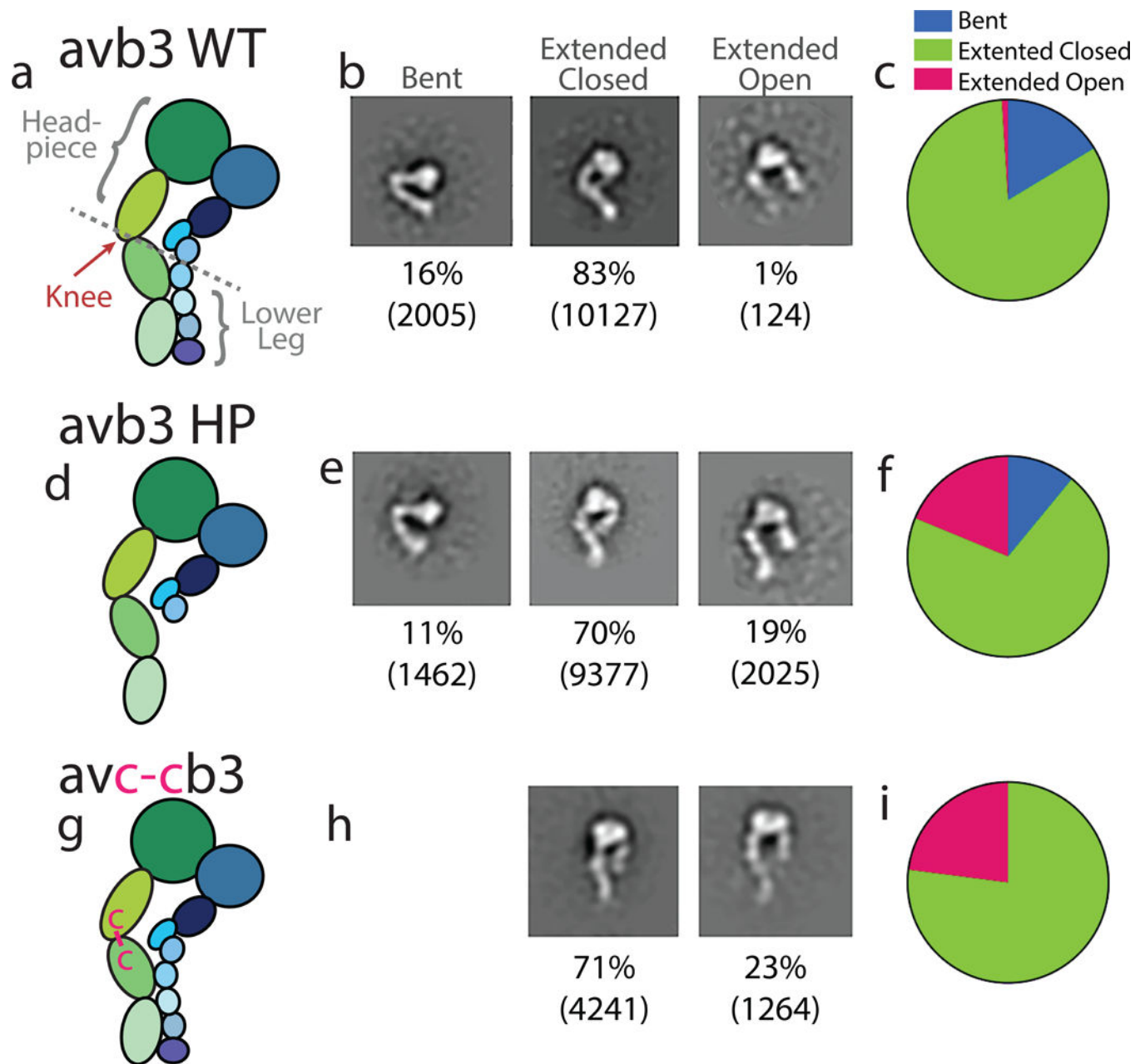
**Figure 3 |. The αv-leg stabilizes integrin extension of the αvβ3 integrin**

a–c, Schematic of the wild type (WT) αvβ3 (**a**), αvβ3-lower leg truncation (αvβ3 HP) (**b**), and αvc-cβ3 (**c**) ectodomains and nomenclature with representative ns-EM class averages of bent, en face extended-closed and extended-open conformations (**b, e, h**), and a pie chart representing percentages of each conformation (**c, f, i**). Below each 2D class average is the percentage of particles belonging to that conformation and the number of particles in parentheses.
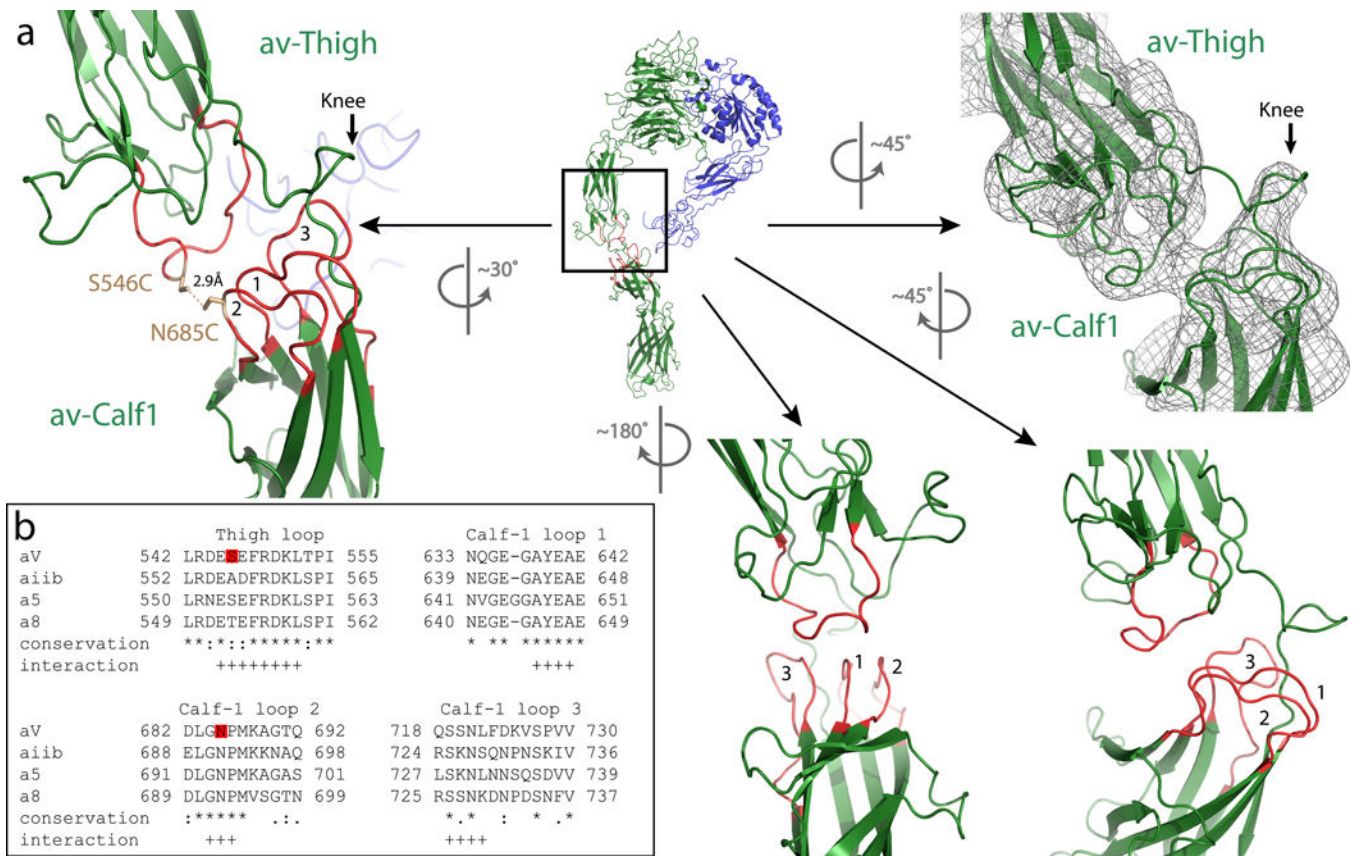
Figure 4 |. The stabilizing mechanism of the extended αv-integrin

a, Ribbon model of the αvβ8 ectodomain subclass (i), en face, from Fig. 2 with the knee region indicated by a box. The corresponding rotated EM density map is shown in the right panel, and the enlarged ribbon model showing a different rotational view to facilitate depiction of the interacting loops 1–3 from the αv-calf-1 with the single loop from the αv-thigh (left panel). The locations of the S546C and N685C mutations and the distance between them are indicated. Additional rotated views and locations of loops are shown in the lower middle and right panels. **b**, The sequence alignment of the amino acid loops of the αv-thigh and αv-calf-1 loops 1–3 of human αv with human α$_{iib}$, α5 and α8 are shown. Red boxes indicate the location of S546C and N685C. Sequence conservation is indicated as follows: * fully conserved amino-acids, : strongly conserved amino-acids, . weakly conserved amino-acids. Putative residues participating in the loops interaction are indicated by +.
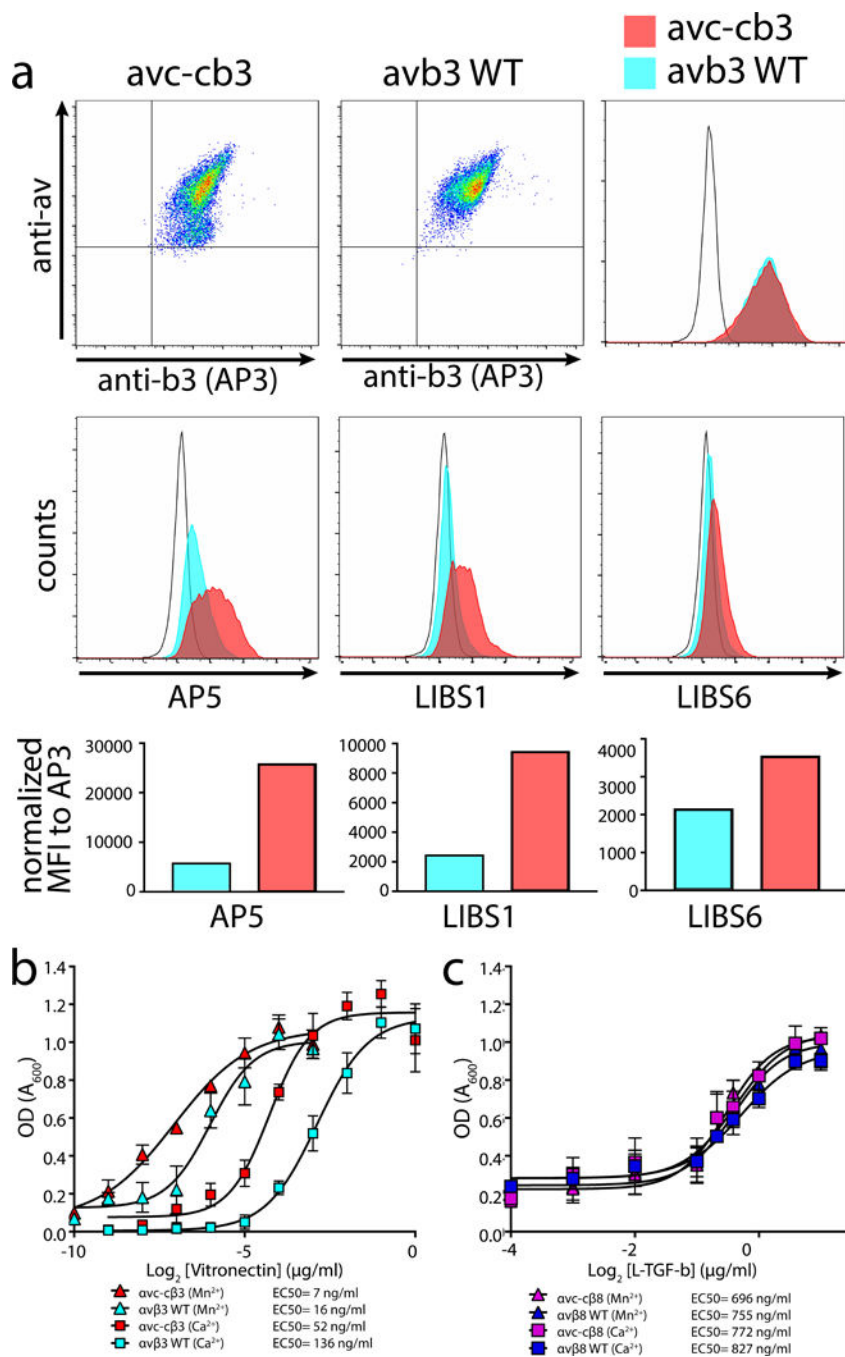
Figure 5 |. The extended αvβ3 integrin shows increased ability to mediate adhesion
a, Expression of full-length human αvc-c (left upper panel) or αv (middle upper panel) paired with β3 in CHOLec 3.2.8.1 cells and detected using anti-human αv or anti-β3 (AP3) monoclonal antibodies, as indicated. Upper right, histogram overlay of β3 staining shows complete overlap of αvc-cβ3 (red) with αvβ3 (blue) compared to mock transfected CHOLec 3.2.8.1 cells (unfilled histogram). Middle panels, ligand-induced binding site (LIBS) antibodies staining sorted pools of αvc-cβ3 or αvβ3 shown in upper panels. AP5 (left), LIBS1 (middle), and LIBS6 (right) compared with mock transfected CHOLec 3.2.8.1 cells

(unfilled histogram). Bottom panels show bar graphs of mean fluorescence intensity (MFI) of each antibody staining $\alpha vc\text{-}c\beta 3$ or $\alpha v\beta 3$ transfected CHOLec 3.2.8.1 cells. **b**, Adhesion assays of $\alpha vc\text{-}c\beta 3$ or $\alpha v\beta 3$ CHOLec 3.2.8.1 transfected cells to wells coated with vitronectin at various concentrations in the presence of basal (Ca^{2+}) or activating cation conditions (Mn^{2+})(n = 3 independent experiment. Data and error bars represent mean $\pm$ s.e.m.). The data was subtracted by mock cell background adhesion. Legend shows the individual EC_{50} values. **c**, Adhesion assays of $\alpha vc\text{-}c\beta 8$ or $\alpha v\beta 8$ CHOLec 3.2.8.1 transfected cells to wells coated with L-TGF-β at various concentrations in the presence of basal (Ca^{2+}) or activating cation conditions (Mn^{2+}) (n=3 independent experiment. Data and error bars represent mean $\pm$ s.e.m.). The source data of the graphs shown in b and c is provided as supplementary material.